IEEE Access
Multidisciplinary | Rapid Review | Open Access Journal

SPECIAL SECTION ON MILLIMETER-WAVE AND TERAHERTZ PROPAGATION, CHANNEL MODELING AND APPLICATIONS

Received October 30, 2019, accepted November 21, 2019, date of publication December 18, 2019, date of current version January 16, 2020.

Digital Object Identifier 10.1109/ACCESS.2019.2960614

An Indoor Channel Model for High Data-Rate Communications in D-Band

L. POMETCU AND R. D'ERRICO, (Senior Member, IEEE)
The French Alternative Energies and Atomic Energy Commission (CEA), 38054 Grenoble, France
University of Grenoble-Alpes, 38400 Saint-Martin-d'Hères, France

Corresponding author: R. D'Errico (raffaele.derrico@cea.fr)

ABSTRACT This paper proposes a measurement based modeling of D-band indoor channels. Different indoor environments were considered including Line-of-Sight (LOS) and Non Line-of-Sight (NLOS) conditions. Double steering at the transmitter and receiver sides was performed allowing angular characterization of the channel. Path loss, delay spread, angular spread, intra- and inter- cluster characteristics were also modeled. These characteristics were then compared to the ones obtained in other millimeter wave bands for the same environment.

INDEX TERMS Channel models, mm-wave, propagation, sub-THz.

I. INTRODUCTION

Nowadays, the development of 5G networks at millimeter-Wave (mm-Wave) bands is motivated by the increasing demand on high data rate. To fully exploit the potentiality of these 5G technologies, reliable channel models are needed. For this reason, a plethora of works was carried out, in the least years, in different frameworks.

The IEEE 802.15.3c task group proposed an mm-Wave channel model [1] based on the extension of the classical Saleh-Valenzuela (V-H) [2] expression for wideband indoor scenarios. In the framework of IEEE 802.11ad, a model was proposed for indoor short-range communications using the 60 GHz unlicensed band [3]. Different research projects, such as METIS [4], MiWEBA [5], mmMagic [6], and works from academia [7], were developed to model the 5G propagation in centimeter and millimeter waves for many scenarios including street-canyon outdoor cellular environment, open-square in shopping malls, open/closed indoor office environments as well as stadiums. Eventually, these works were considered in the framework of 3GPP standardization [8].

Going beyond the needs of 5G networks, sub-THz frequencies were envisioned for (ultra) dense deployments of access points within 10 meters of the Line Of Sight (LOS) communication range.

In fact, it is well known that absorption by atmospheric gases is a significant factor throughout the band and it increases with frequency, presenting a few specific absorption lines, mainly those of oxygen at 60 GHz and water vapors at 24 GHz and 184 GHz. In the frequency windows between these absorption peaks, mm-Waves suffer less atmospheric attenuation. Hence the peak attenuations, which are in the order of dB/km, can be neglected for short ranges of a few meters [9].

Above 100 GHz, the literature on channel modeling is mainly focused on indoor scenarios at few meters. In [10] various measurements were conducted in both LOS and Non Line-of-sight (NLOS) scenarios. The path loss, MIMO capacity and shadowing effects were extracted in between 260 GHz and 400 GHz but a channel model has not been provided. The "desktop" scenario was considered in [11] and [12], and the authors extracted the path loss and shadowing characteristics in the 300 – 320 GHz frequency range. A sub-THz channel at 300 GHz for small indoor scenarios was also investigated in [13] and [14], providing the path loss, angles of arrival characteristics, and addressing the effect of the antenna misalignment [15].

The D-band channel was characterized in [16] for small transmitter - receiver distances, i.e. up to 90 cm. Different types of blockage were considered using different objects (e.g. glass beaker, plastic cup and ceramic mug). It was shown that the LOS path loss was around 75 dB and the delay spread was about 0.031 ns. For the NLOS case, depending on the considered blockage, the authors in [16] obtained a path loss between 77 dB and 88 dB, and a delay spread varying from 0.016 ns to 0.064 ns.

In this paper, we address a portion of the D-band, more precisely between 126 and 156 GHz. With respect to

The associate editor coordinating the review of this manuscript and approving it for publication was Reiner Thomä.

literature, we study indoor scenarios at higher distances up to 10.6 m. The channel model proposed here is based on the extended Saleh-Valenzuela (S-V) model. Our motivation for choosing this model relies mainly on the assumptions made on the frequency range, stochastic properties of the positions of the receiver and transmitter and on the indoor environment scenarios. Furthermore, it was found that measurements of ultra-wideband (UWB) channels also fit with the S-V model very well. Even if in [17] it was demonstrated that path clustering is not apparent in the angular-delay domain, the authors determined that a clustering behavior is present even if most paths exist alone. Other studies have also been done at mm-Wave frequencies (IEEE 802.15.3c [1], IEEE 802.11ad [3]) that are based on the extended time-angular S-V model and considered that the model is cluster based. At the same time, we wanted to also be able to compare our results with the ones presented in [18] that are part of the mmMagic initiative [6] and that used the same approach to characterize their measurements. In this article, blocking scenarios from humans, doors and partitions were also considered. According to the authors' knowledge, this has not yet addressed in literature. Channel measurement methodology allowed the characterization of not only the large-scale parameters, but also of the multi-path and clusters characteristics. Thanks to double steering at both the transmitter and receiver sides, the Angle of Arrival (AoA) and Angle of Departure (AoD) characteristics are obtained.

The article is structured as follows: Section II presents the channel measurement setup along with the scenarios considered. In Section III, the channel characteristics and model are provided for both LOS and NLOS scenarios. Section IV compares the measured channel characteristics with those obtained in the E and V bands under the same environment conditions [18], as well as with other mm-Wave indoor models. Finally, Section V concludes the paper and gives an outlook for future works.

II. CHANNEL MEASUREMENT CAMPAIGN

A. SETUP OVERVIEW

The measurement setup is shown in Fig. 1. It consists of a 4-port Vector Network Analyzer (VNA) connected to two antennas representing the transmitter (Tx) and receiver (Rx), respectively, via two Rohde & Schwarz mm-Wave converters ZC170. Two antenna positioners, with a precision of 0.01 mm in translation and 0.1° in angle, were used allowing antenna steering. The transmitting (Tx) antenna was placed on a 1-axis (azimuth) positioner, while the receiving (Rx) antenna was mounted on a 3-axis (x-y-Φ) positioner. During the measurement campaign, the Rx positioner performs a spatial grid of x-y-Φ for each Tx position. Two linearly polarized horn antennas with a gain of 20 dBi were employed [19]. An external laptop was used to control the VNA acquisitions and the two positioners through Ethernet cables.

The sounded band spans from 126 to 156 GHz, by step of 10 MHz, i.e. 3001 points. The output power was set to 12 dBm and the intermediate frequency bandwidth (IFBW) was chosen equal to 100 Hz. The dynamic range of the sounder is typically 105 dB, which corresponds at the highest frequency to the free space path loss at 30 m.

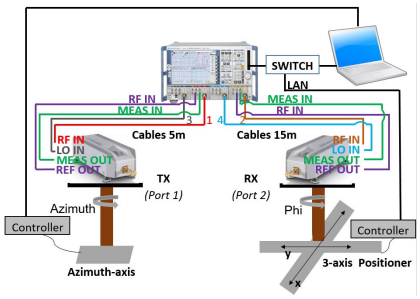

FIGURE 1. Measurement setup.

B. MEASUREMENT CAMPAIGNS

Three measurement campaigns were conducted in indoor premises at CEA-LETI and they are presented in Fig. 2 as *Indoor 1*, *Indoor 2* and *Indoor 3*. *Indoor 1* environment consists of a laboratory where a number of usual scatterers like tables, chairs and closets are present. The total dimensions of the room are $4.3 \times 7 \times 3$ m^3. *Indoor 2* environment is a conference room of $6 \times 25.77 \times 3$ m^3. The antennas were placed there, in the middle of the room, between the tables. *Indoor 3* environment is an ordinary office, whose dimensions are $7 \times 7 \times 3$ m^3.

LOS measurements were performed up to 10.6 m. This distance was considered only in *Indoor 2* scenario, because of the room dimensions. Fig. 2(d) shows the locations of the receiver as colored dots. At each receiver location, the x-y-Φ positioner moved linearly in two directions and made a full azimuth rotation from −180° to 180° using a step of 20°. On the transmitter side, the steering was performed between −170° and 170° (step of 20°) because of a mechanical limitation of the positioner. This angular step values on the transmitter/receiver sides were chosen considering the average half power beam width (HPBW) for the maximum antenna directivity measured in anechoic chamber [19]. It can be observed in Fig. 2(d) that, the receiver (see legend: Rx positioner) has been moved over the x- and y- axes depending on each scenario considered. For *Indoor 2* scenario (Fig. 2(d)) the head of the positioner (green, blue, cyan, red, violet, grey dots), where the antenna was placed, has been displaced over the axes in the following manner: x-axis displacement in the center of the positioner and y-axis displacement of 0 m and 0.8 m from the origin of the positioner. Similar types of displacements have been considered for the two other scenarios: *Indoor 1* scenario: x-axis displacement of 0 m and 0.4 m, y-axis displacement of 0 m, 0.4 m and 0.8 m; *Indoor 3* scenario: x-axis displacement of 0 m, 0.4 m and 0.8 m, y-axis displacement of 0 m and 0.4 m.

In the NLOS scenarios, we considered different obstruction conditions, as depicted in Fig. 3. A human phantom was used in *Indoor 1* to realize human body obstruction at

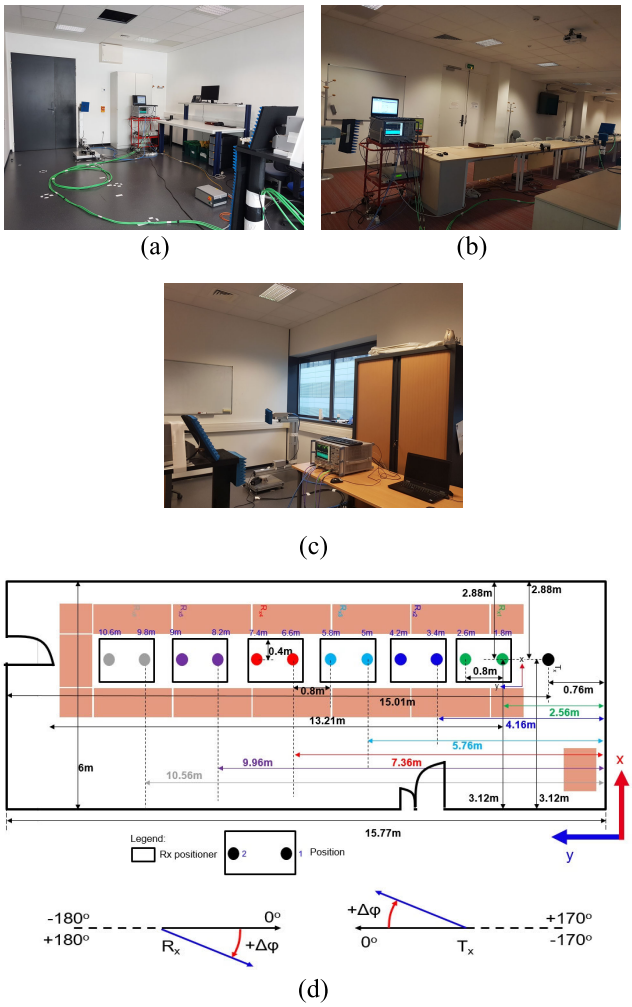

FIGURE 2. LOS measurement scenarios: (a) *Indoor 1* scenario (laboratory), (b) *Indoor 2* scenario (conference room), (c) *Indoor 3* scenario (office) and (d) Floor plan of the *Indoor 2* scenario with measurement grids.

different positions. An 11 cm thick wall (plasterboard) and a 5 cm thick door adjacent to the office of *Indoor 3* scenario were also considered as blockage. Measurements were performed, there, considering a relative distance between terminals going from 1 m to 3 m, always respecting the far-field condition. Actually, the horn antenna size is 8.5 × 6.4 mm^2, which gives at the highest frequency (156 GHz) a Fraunhofer distance equal to 11.7 cm.

The human phantom used is a CTIA compliant human torso phantom [20] that is usually employed for Over-The-Air (OTA) tests up to 6 GHz. The human body represents one of the major causes of link obstruction for indoor environments but only a few studies have been realized at mm-Wave bands [21]–[23]. Usually, the human body shadowing at mm-Wave frequencies is about 20-30 dB [21], [23], [24]. In [25] a cylinder has been used as simulation obstruction at 60 GHz resulting in a 15-20 dB blocking loss. Another study [26] has been done also at 60 GHz but this time using the human body as obstruction and a 12-22 dB loss has

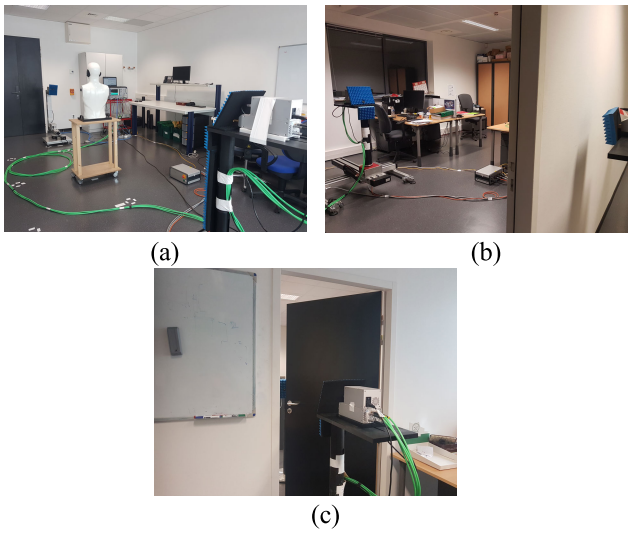

FIGURE 3. NLOS measurement scenarios: (a) human body blocking, (b) wall obstruction and (c) door obstruction.

been obtained. The results have been validated by human-based shadowing measurements. Depending on the type of obstruction used, a maximum of 35 dB blocking loss has been obtained by using a human leg in [23].

Because the characteristics of the phantom used here were unknown at sub-THz frequencies, a cross-check measurement was realized to compare the human body characteristics with the ones given by the phantom in the frequency band of interest. The transceiver and receiver antennas were placed at 1 m distance and the phantom was moved along 14 positions in between the antennas (Fig. 4(a)). The same measurement was repeated with a real human subject. Fig. 4(b) compares the blocking losses in the two cases, showing a good agreement between the two sets of measurements, validating in a first order approximation, the use of the phantom for channel sounding purposes at the frequencies of interest. A blocking loss of maximum 22 dB has been obtained when the phantom/human body was placed directly in between the transmitter and the receiver thus being in concordance with literature.

III. CHANNEL CHARACTERIZATION

A. LOS SCENARIOS

The channel impulse response can be expressed as follows:

$$h\left(\tau, \Phi^T, \Phi^R\right) = \sum_{k=1}^{K} \alpha_k \cdot \delta\left(\tau - \tau_k\right) \cdot \delta\left(\Phi^T - \Phi_k^T\right) \cdot \delta\left(\Phi^R - \Phi_k^R\right) \quad (1)$$

where $\alpha_k, \tau_k, \Phi_k^T, \Phi_k^R$ represent the amplitude, delay, angle of departure and angle of arrival of the kth multipath component (MPC), respectively. The MPCs were extracted from the bidirectional channel measurements by synthetizing the omnidirectional Power Angular Delay Profile (PADP) [17], [18]. Fig. 5 presents an example of PDP for *Indoor 1* scenario when

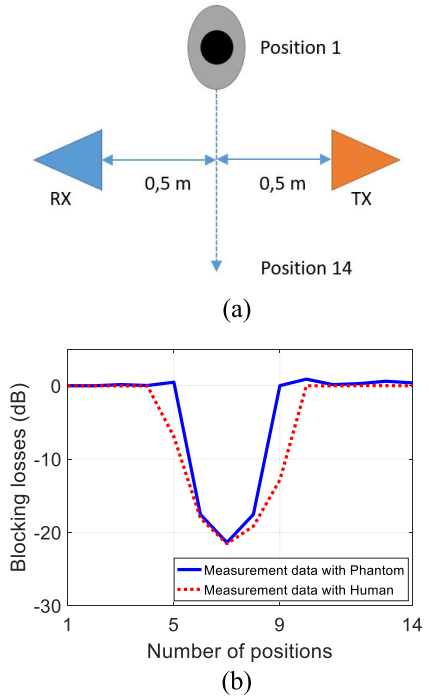

FIGURE 4. Measurement with phantom and human body: (a) scenario and (b) blocking loss.

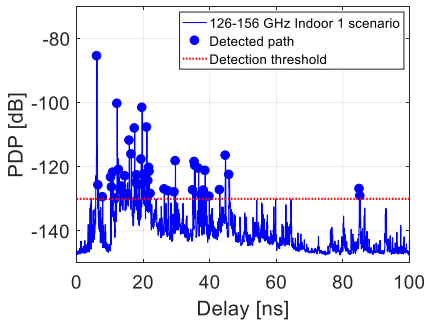

FIGURE 5. Example of PDP and estimated multipath for *Indoor 1* scenario.

the distance in between the antennas is of 1.8m, Φ is equal to 0° at the receiver side and the Azimuth angle at the transmitter side is 0°.

The MPC detection threshold was chosen 20 dB above the noise floor. An example of AoD and AoA for *Indoor 1* scenario is shown in Fig. 6. Each point is an estimated MPC, whose color represents the amplitude, while the radial distance represents the time of arrival, here traduced in meters. The AoD/AoA correspond to the direction of radiation of the Tx/Rx as it can be observed in Fig. 2(d).

1) LARGE SCALE CHARACTERISTICS

a: PATH LOSS MODEL

Starting from the experimental results the path loss model is extracted using the floating intercept point model:

$$PL\,(d)\,[dB] = PL_0 + 10 \cdot n \cdot \log_{10}\left(\frac{d}{d_0}\right) + X_\sigma \qquad (2)$$

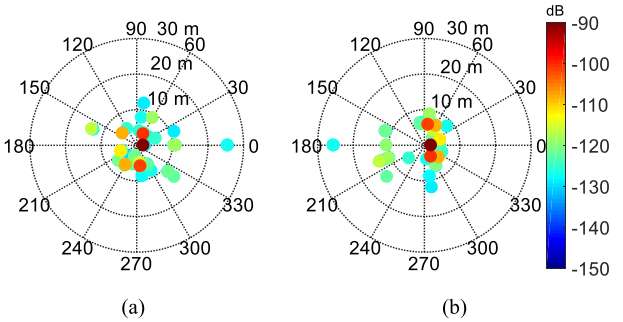

FIGURE 6. *Indoor 1* scenario: (a) AoD and (b) AoA.

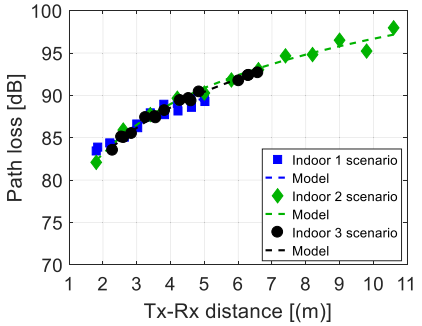

FIGURE 7. Path loss for all three LOS scenarios.

TABLE 1. Path loss parameters model.

Scenario	PL_0 [dB]	n	X_σ [dB]
Indoor 1 scenario	79.6	1.45	0.47
Indoor 2 scenario	77.4	1.93	0.6
Indoor 3 scenario	77	1.91	0.25

where PL_0 represents the intercept point at $d_0 = 1$m, n is the path loss exponent, d represents the real distance in between the transmitter and receiver and X_σ is the standard deviation due to large scale variation effects. Fig. 7 presents the path loss and the model depending on the relative distance between the Tx and Rx for all three indoor scenarios considered. The parameters of the model are listed in Table 1. The path loss exponent shows a behavior very close to free space in *Indoor 2 and 3* scenarios, while in *Indoor 1* it seems closer to classical indoor values.

b: DELAY AND ANGULAR DISPERSION PROPERTIES

From the MPCs, the delay spread and angular spread have been estimated. Fig. 8(a) exhibits the delay spread for the three indoor scenarios. As seen, the delay spread does not exceed 15 ns. For *Indoor 2* scenario, a decrease of the delay spread can be observed after 5.8 m. This decrease after 5.8 m can be explained by the fact that, for large distances, the weak multipath components disappear below the noise floor resulting in a decrease of the delay spread. Also, a higher delay spread is obtained from the *Indoor 2* scenario because of the larger distances in between the Tx-Rx system and the

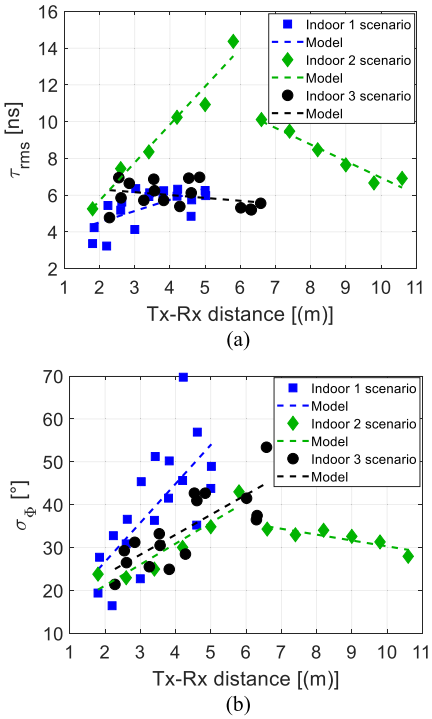

FIGURE 8. Display of: (a) Delay spread and (b) angular spread for all indoor LOS scenarios.

dimensions of the room. It can also be observed in Fig. 8 that the delay spread and angular spread increase with the increase of the Tx-Rx distance in between 1.8 m and 5.8 m for all three scenarios. This behavior can be explained by the fact that the earliest arriving multipath components are attenuated and they do not dominate the delay spread over the later arriving components till 5.8 m. Furthermore, this leads to the conclusion that the path loss, delay spread and angular spread are correlated in between 1.8 m and 5.8 m. Even if the delay spread and angular spread depend on the environment, similar behaviors have been observed in other propagation environments [17], [27]–[29]. In order to model this *Indoor 2* behavior we have used an intercept point model with a breaking point as described in (5) for the delay spread and in (6) for the angular spread.

The delay spread and angular spread dependency along distance were modeled according to the following expressions:

$$\tau_{rms}[ns] = a1 \cdot d + b1 \tag{3}$$

$$\sigma_\Phi(deg) = c1 \cdot d + e1 \tag{4}$$

$$\begin{cases} \tau_{rms1}\,[ns] = a1 \cdot \left(\dfrac{d}{d_0}\right) + b1, & d \le d1 \\ \tau_{rms2}\,[ns] = a2 \cdot \left(\dfrac{d}{d_1}\right) + b2, & d > d1 \end{cases} \tag{5}$$

$$\begin{cases} \sigma_\Phi(\text{deg}) = c1 \cdot \left(\dfrac{d}{d_0}\right) + e1, & d \le d1 \\ \sigma_\Phi(\text{deg}) = c2 \cdot \left(\dfrac{d}{d_1}\right) + e2, & d > d1 \end{cases} \tag{6}$$

where a is the delay spread exponent, b represents the standard deviation, c is the angular spread exponent, e is the standard deviation and $d1$ represents the measurement distance in between Tx and Rx where the delay/angular spread are maximum (here 5.8 m for *Indoor 2* scenario).

Equations (3)-(4) correspond to *Indoor 1* and *Indoor 3* scenarios and (5)-(6) correspond to *Indoor 2* scenario. While there is no clear distance dependency for delay spread, one can distinguish a clear trend for angular spread. The model parameters are listed in Table 2.

TABLE 2. Delay spread and angular spread model parameters.

Scenario	$a1$ [ns/m]	$b1$ [ns]	$a2$ [ns/m]	$b2$ [ns]	$c1$ [deg/m]	$e1$ [deg]	$c2$ [deg/m]	$e2$ [deg]
Indoor 1 scenario	0.6	3.3	[-]	[-]	9.1	8.5	[-]	[-]
Indoor 2 scenario	2.068	1.6	-0.9	16	4.9	11.4	-1.4	44
Indoor 3 scenario	0.15	6.6	[-]	[-]	4.7	14.4	[-]	[-]

2) CLUSTER CHARACTERISTICS

Usually paths arrive in clusters that are sets of multipath that have similar propagation characteristics like delays or angles of arrival or departure. Here, the paths have been grouped in clusters using the K-PowerMeans algorithm [30], which uses the multipath component distance (MCD) as a metric to identify the clusters. The equation for determining MCD is:

$$MCD^{i,j} = \sqrt{\left\|MCD^{i,j}_{AoA}\right\|^2 + \left\|MCD^{i,j}_{\tau}\right\|^2} \tag{7}$$

with:

$$MCD^{i,j}_{AoA} = \frac{1}{2}\left|a_i - a_j\right| \tag{8}$$

and

$$MCD^{i,j}_{\tau} = \zeta \frac{\left|\tau_i - \tau_j\right|}{\Delta\tau^2_{max}}\tau_{std} \tag{9}$$

where $MCD^{i,j}_{AoA}$ represents the MCD of the angles of arrival, $MCD^{i,j}_{\tau}$ is the MCD of the delay in the azimuth plane, $a_k = [\sin(\theta_k)\cos(\Phi_k), \sin(\theta_k)\sin(\Phi_k), \cos(\Phi_k)]^T$, τ_{std} is the standard deviation of the delays, $\Delta\tau_{max} = \max_{ij}\left(\left|\tau_i - \tau_j\right|\right)$, and ζ represents a delay scaling factor that sets the importance of the delay. For this study, we have used $\zeta = 1$ giving the angular and delay domains a comparable weight. Moreover, we have considered that the power of an identified cluster should be at least 0.1% of the total determined power in order to avoid the detection of unnecessary clusters.

a: MULTIPATH CLUSTERING RESULTS

An example of clustering using the K-PowerMeans algorithm is shown in Fig. 9, where each color represents a different cluster, while the yellow dot is the cluster centroid. The cyan colored symbols represent isolated paths that present very different propagation distances from all other paths so they

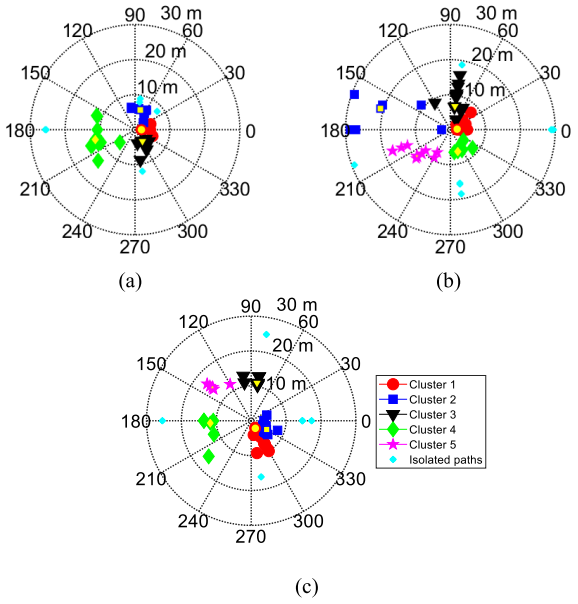

FIGURE 9. Example of multipath clustering for various positions in the indoor environments (The yellow marker shows the centroid of the corresponding cluster): (a) *Indoor 1*, (b) *Indoor 2* and (c) *Indoor 3* scenarios.

cannot be included in the clusters. These paths have been determined following the threshold:

$$\tau_{k\ isolated\ paths} > \tau_{k,centroid} + 3 \cdot c^{l}_{DS} \tag{10}$$

where $\tau_{k,centroid}$ represents the delays of the centroids for each cluster and c^{l}_{DS} represents the delay spread of the cluster (12). All paths that presented higher delays than $\tau_{k,centroid} + 3 \cdot c^{l}_{DS}$ were considered as isolated and were not take into account. This threshold was empirically chosen among other values (e.g. two or four times the cluster delay spread) in order to encompass all important paths in a cluster. The process of the determination of the isolated paths consist in first running the K-PowerMeans algorithm for all paths, after detect the paths that respect the threshold above and finally re-run the K-PowerMeans algorithm again without these isolated paths.

In all three LOS scenarios, five clusters appear with the highest likelihood. While the first cluster appears along the LOS direction, the following ones are due to specular reflections from the walls and objects in the studied environments. It is known that for LOS conditions, the majority of the multipath appears from the LOS path and first order reflections over large surfaces. Our results are comparable with the ones presented in [18], [31], [32] where a maximum of 6 clusters were obtained at 60 GHz and of 4 clusters at 73 GHz and 80.5-86.5 GHz for indoor/outdoor scenarios. Furthermore, 2 - 5 clusters were obtained at 28 GHz only for indoor channel measurements [33].

Fig. 10 shows the energy contribution of the LOS cluster over the total power. We can see that the LOS cluster presents the highest received power and that the total power is highest for the *Indoor 3* scenario. This can be explained by the fact

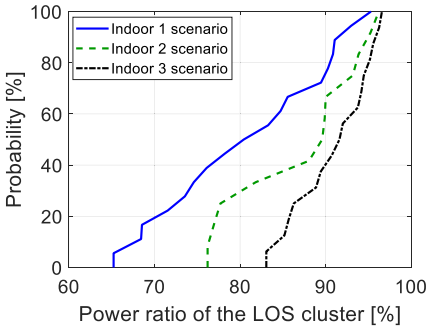

FIGURE 10. Cumulative distribution function of the LOS cluster contribution over the total power.

that in the third scenario we have multiple scatterers located near the receiver that contribute to the total power.

b: INTRA-CLUSTER LARGE-SCALE PARAMETERS

In this section, we determine for each cluster the root mean square (rms) delay spread and angular spread. The so-called intra-cluster rms delay spread of cluster "l" will be denoted c^{l}_{DS} and the rms of the angular spread c^{l}_{ASA}. For a cluster "l", the rms is determined based on the powers, AoAs, and delays of the resolvable paths of the specified cluster and they are expressed as:

$$c^{l}_{ASA} = \sqrt{\frac{\sum_{k=1}^{K_l} \left(\Phi_k - \bar{\Phi}_l\right)^2 \alpha_k^2}{\sum_{k=1}^{K_l} \alpha_k^2}} \tag{11}$$

$$c^{l}_{DS} = \sqrt{\frac{\sum_{k=1}^{K_l} \left(\tau_k - \bar{\tau}_l\right)^2 \alpha_k^2}{\sum_{k=1}^{K_l} \alpha_k^2}} \tag{12}$$

where $\bar{\Phi}_l$, $\bar{\tau}_l$ are the mean angle and delay of the cluster "l", respectively, and K_l is the number of multipath in the cluster. Table 3 lists the cluster's rms angular and delay spread values for the different Rx locations in the three scenarios. For each Rx location, each parameter is calculated by averaging the values obtained for all positions at that location. It can be observed that for the first cluster, the rms delay spread is quite constant over the Rx locations for all environments. Namely, a mean rms delay spread of the first cluster of about 14.48 ns, 4.82 ns and 10.62 ns are obtained in the studied frequency band for *Indoor 1*, *Indoor 2* and *Indoor 3* scenarios, respectively. The rms delay spreads for the first and last scenarios are similar because the measurements were performed for similar maximum relative distances between end nodes. A mean rms angular spread for the first cluster of about 63.6° (*Indoor 1*), 70.7° (*Indoor 2*), 14° (*Indoor 3*) are obtained for the environments. The rms angular spread of *Indoor 3* scenario is lower than that of the first two scenarios because of the multiple sources of reflections located in the vicinity of the receiver that result in a higher received power.

The statistics of the intra-cluster large scale parameters have also been determined and they are shown in Fig. 11.

TABLE 3. Average rms angular and delay spreads per cluster.

Cluster number		*1st cluster*		*2nd cluster*		*3rd cluster*		*4th cluster*		*5th cluster*	
Scenarios		$\bar{c}_{ASA}$ [°]	$\bar{c}_{DS}$ [ns]	$\bar{c}_{ASA}$ [°]	$\bar{c}_{DS}$ [ns]	$\bar{c}_{ASA}$ [°]	$\bar{c}_{DS}$ [ns]	$\bar{c}_{ASA}$ [°]	$\bar{c}_{DS}$ [ns]	$\bar{c}_{ASA}$ [°]	$\bar{c}_{DS}$ [ns]
Indoor 1 scenario	Rx1	32.16	12.74	9.39	5.17	9.20	3.0	13.81	5.52	7.04	2.78
	Rx2	73.3	11.83	12.08	7.07	4.5	3.85	13.23	4.56	[-]	[-]
	Rx3	36.17	10.03	7.77	9.1	5.84	2.13	25.08	3.1	[-]	[-]
	Rx4	112.77	23.31	24.24	9.36	14.92	5.11	12.26	3.63	9.2	1.44
Indoor 2 scenario	Rx1	24.65	4.9	10.25	16.43	3.76	7.13	13.66	4.53	14.88	14.41
	Rx2	15.78	6.24	15.14	10.65	16.58	6.15	16.01	14.95	[-]	[-]
	Rx3	60.10	3.25	7.92	5.88	8.96	4.17	14.06	7.03	6.99	4.1
	Rx4	100.77	4.92	10.98	2.65	8.44	5.28	6.0	7.21	16.37	6.5
	Rx5	64.45	5.41	8.57	9.3	9.98	8.9	5.0	3.87	5.41	3.2
	Rx6	158.48	4.22	3.72	2.56	10.24	11.28	7.23	2.3	9.97	3.8
Indoor 3 scenario	Rx1	7.12	12.51	42.3	1.73	9.56	11.02	9.9	4.41	12.04	5.0
	Rx2	8.12	14.56	117.61	8.67	2.73	3.48	5.12	4.96	10.48	4.32
	Rx3	20.66	9.39	5.57	20.28	9.86	5.19	9.46	5.88	18.22	3.2
	Rx4	22.46	13.53	15.86	6.35	13.75	5.75	13.96	3.10	[-]	[-]
	Rx5	26.31	8.47	8.78	5.73	3.61	3.98	10.84	2.76	[-]	[-]
	Rx6	16.94	7.91	5.42	7.42	11.54	8.24	10.15	3.56	8.99	4.01
	Rx7	6.56	9.66	13.34	4.5	18.28	8.42	[-]	5.47	[-]	0.1
	Rx8	4.33	8.94	14.13	2.38	8.51	5.99	5.66	7.27	17.16	6.26

[-] – Cluster does not exist; Rxi - represents the receiver placement at position i (see Fig.2(d))

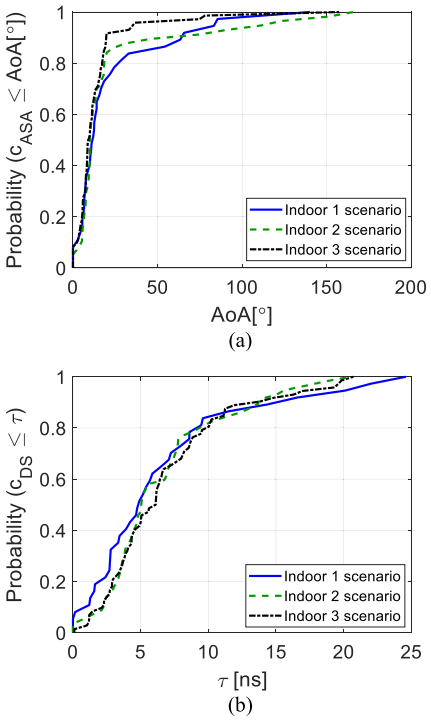

FIGURE 11. Cumulative distribution function of intra-clusters: (a) rms angular spread and (b) rms delay spread for the three scenarios.

As seen, a mean value for the rms angular spread of 12° for *Indoor 1*, 10° for *Indoor 2* and 9° for *Indoor 3* and the intra-cluster rms is higher for the *Indoor 3* scenario. By doing the Kolmogorov-Smirnov (KS) test we have seen that the values of c^l_{ASA} do not follow the same probability distribution. For the rms delay spread we obtained a mean value of 4.9 ns (*Indoor 1*), 5.05 ns (*Indoor 2*) and 6.11 ns (*Indoor 3*) for each environment.

c: SPACE-TIME STATISTICAL CHANNEL MODELLING

Here we considered an extended version of the Saleh-Valenzuela (S-V) model, as follows:

$$h(t,\phi) = \sum_{l=0}^{L}\sum_{k=0}^{K_l} \beta_{kl} e^{j\Phi_{kl}} \cdot \delta(t - T_l - \tau_{kl}) \cdot \delta(\Phi - \Theta_l - \phi_{kl}) \quad (13)$$

with l and k are the cluster and path indexes, L and K_l are the number of the cluster and the sub-path in cluster "l", respectively. T_l is the arrival time of the lth cluster while β_{kl}, Φ_{kl}, τ_{kl} and ϕ_{kl} are the amplitude, phase, arrival delay and azimuth AoA of the kth path in the lth cluster, respectively. The path gain is modeled as follows:

$$\overline{\beta^2_{kl}} = \overline{\beta^2(T_l, \tau_{kl})} = \overline{\beta^2(0,0)} e^{-\frac{T_l}{\Gamma}} e^{-\frac{\tau_{kl}}{\gamma}} \quad (14)$$

where $\beta^2(0,0)$ is the average power of the first arrival of the first cluster and Γ and γ are the power-delay time constant of the cluster and rays, respectively.

We have assumed that the clusters and rays arrival rate follow a Poisson distribution with fixed Λ cluster arrival and λ ray arrival rates:

$$p(T_l \,|T_{l-1}) = \Lambda e^{-\Lambda(T_l - T_{l-1})}, \quad l > 0 \quad (15)$$

$$p\left(\tau_{kl} \,|\tau_{(k-1)l}\right) = \lambda e^{-\lambda(\tau_{kl} - \tau_{(k-1)l})}, \quad k > 0 \quad (16)$$

Fig. 12 presents the clusters and rays arrival rates as well as the clusters and ray decay constants obtained from the measurements in the three environments.

Table 4 summarizes the clusters and rays decay constant and arrival rate average values. In *Indoor 1* and *Indoor 3*

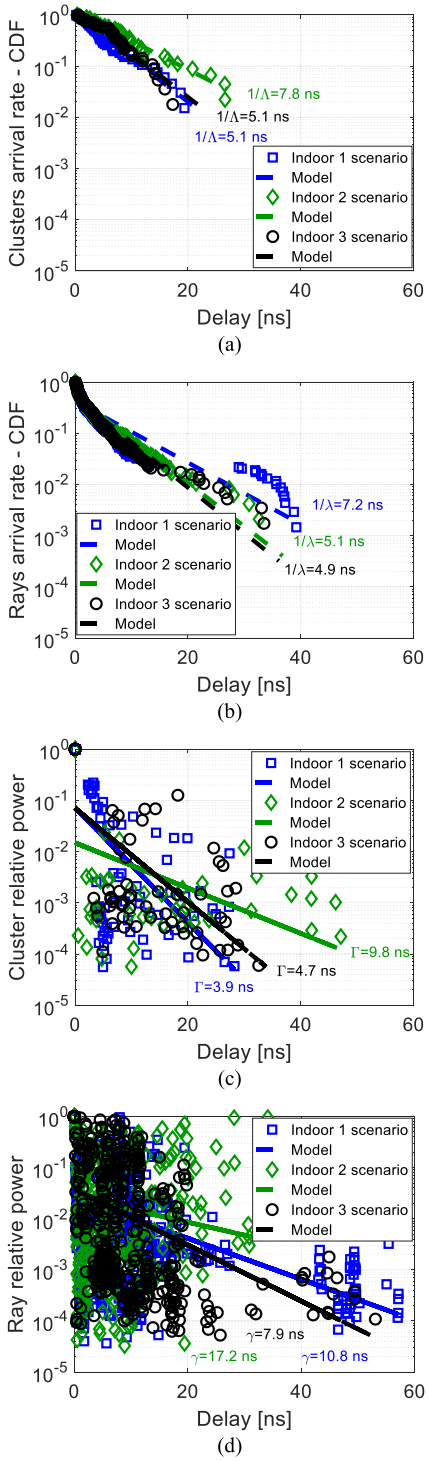

FIGURE 12. Representation of: (a) Clusters arrival rate, (b) Rays arrival rate, (c) Clusters decay constant and (d) Rays decay constant in the three scenarios.

scenarios the clusters and rays decay faster that in *Indoor 2*: this can be explained by the fact that a higher path loss is obtained at higher distances.

We have also determined the distribution of the small scale fading that corresponds to our proposed channel model.

In Fig. 13 we show the CDF of the small scale fading along with two fitting distributions (Rayleigh and Log-Normal). It can be observed that the Log-Normal distribution fits better the fading amplitude in comparison with the Rayleigh distribution, as also witnessed by the log-likelihood, reported in Fig. 13. This behavior can also be explained by the fact that the measurements have been done in a large frequency band. In July 2006, the IEEE P802.15 Working Group for Wireless Personal Area Networks (WPANs) proposed a Saleh-Valenzuela channel model for a library environment [34]. The channel model has also shown that a log-normal distribution may be used for intra-cluster MPC amplitude modeling and that a Rayeligh distribution gives the worse approximation of the empirical data. A similar consideration was done in the framework of channel modelling for UWB. An extensive analysis can be found in [35], where a Nakagami distribution was preferred.

TABLE 4. Decay rate and arrival rate of clusters and rays.

Scenario	Γ [ns]	γ [ns]	$1/\Lambda$ [ns]	$1/\lambda$ [ns]
Indoor 1 scenario	3.9	10.8	5.1	7.2
Indoor 2 scenario	9.8	17.2	7.8	5.1
Indoor 3 scenario	4.7	7.9	5.1	4.9

In Fig. 14 we show an example of distribution for the first position of the receiver for each scenario where the distance in between the two antennas is for *Indoor 1*, *Indoor 2* and *Indoor 3* scenarios equal to 1.8m. The clusters and ray decay rates show that the clusters overlap in time domain.

We can see in Fig. 14(a) that the third cluster (triangles) originates prior to the first cluster (circles). In the *Indoor 2* scenario (Fig. 14(b)) the second cluster (squares) appears before the ending of the first cluster. Here, the first cluster represents the set of multipath that contains the LOS component with the highest received power and highest arrival delay of the MPC and also it contains first order reflections. In general, a current cluster, with the exception of the first cluster, originates prior to the ending of a previous cluster. The cluster's overlap is shown by higher clusters decay constant in comparison to rays decay constant.

Fig. 15 shows the probability density function (pdf) of the intra-cluster rays AoA in the three indoor scenarios. The probability density of the relative azimuth AoAs of the l^{th} ray and k^{th} cluster is determined as follows:

$$pdf\ (\phi_{kl}\,|\mu, \sigma\,) = \frac{1}{\sigma\sqrt{2}} e^{-\frac{\sqrt{2}}{\sigma}|\phi_{kl}-\mu|} \tag{17}$$

where σ and μ denote the standard deviation and mean value of the relative angles of the rays, respectively.

From the results obtained we have seen that a Laplacian distribution is suitable to all three environments studied here. The standard deviation of the relative arrival angle $\sigma = 45°$ for *Indoor 1*, $\sigma = 47°$ for *Indoor 2* and $\sigma = 29°$ for *Indoor 3*.

The maximum log-likelihood has been determined and represented in Table 5 in order to measure the reliability of our Gaussian/Laplacian fitting of the relative azimuth AoAs.

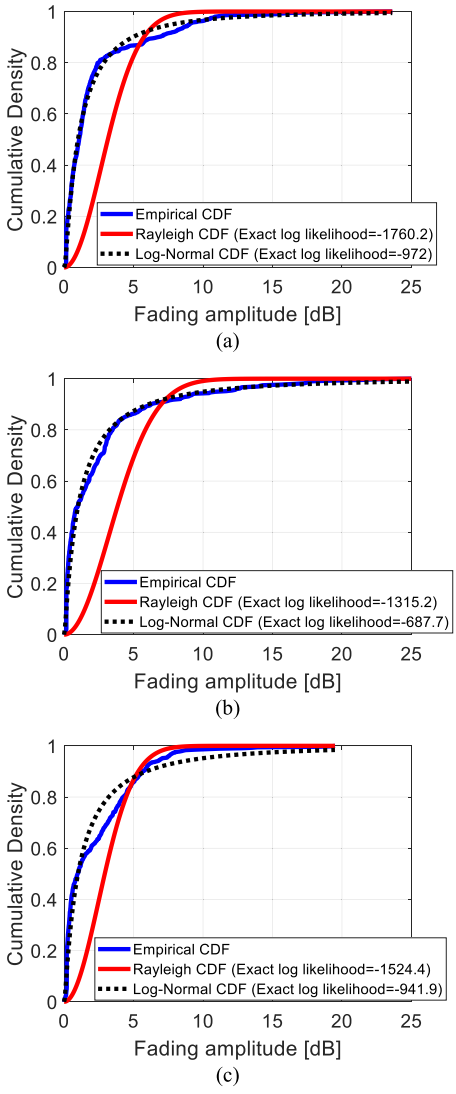

FIGURE 13. CDF of the small scale fading for: (a) Indoor 1, (b) Indoor 2 and (c) Indoor 3 scenarios.

TABLE 5. Maximum log-likelihood.

Scenario	*Gaussian distribution*	*Laplacian distribution*
Indoor 1 scenario	-4021.1	-3887.2
Indoor 2 scenario	-2793.7	-2642
Indoor 3 scenario	-3101.6	-2995.4

For all three scenarios, it can be observed that the Laplacian distribution has a higher maximum log-likelihood estimate in comparison with the Gaussian distribution, which leads to conclude that it is a better fitting for the normal distributed relative arrival angle of the rays.

Fig. 16 presents the Clusters' AoA distribution. The AoAs were transformed from the [−180°-180°] representation to the [0°- 360°] one and after the cdf has been determined. The cdf can be roughly approximated by a straight line in each case, indicating that clusters' AoA is quasi-uniformly distributed in between 0° −358°, 0° −337° and 35° −342° for

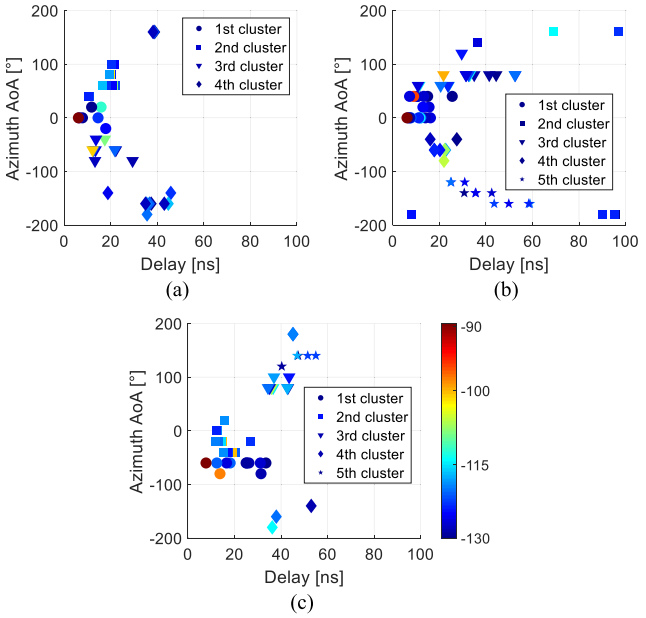

FIGURE 14. Example of overlapping clusters in: (a)*Indoor 1*, (b) *Indoor 2* and (c) *Indoor 3* scenarios.

Indoor 1, *Indoor 2* and *Indoor 3* scenarios, respectively. Note that the distributions are not spread over the entire angular domain from 0° to 360° because the clusters that appear near the reference cluster are considered as part of the reference cluster. In conclusion, the results show that the clusters arrival angles are uniformly distributed over approximatively all the azimuthal angles.

The arrival of clusters and rays are modeled with their pdf's as shown in (15)-(16) but these distributions can be used only for time-only models (ex. original S-V model). In order to extend our model and to also take into account the spatial component, we have introduced the angles of arrival into the model so the pdf's of clusters and rays arrival become dependent of the corresponding arrival angles and are expressed as:

$$p\left(T_l, \Theta_l \left| T_{l-1}, \Theta_0\right.\right) = p\left(T_l \left| T_{l-1}\right.\right) p\left(\Theta_l \left| \Theta_0\right.\right) \quad (18)$$

$$p\left(\tau_{kl}, \phi_{kl} \left| \tau_{(k-1)l}\right.\right) = p\left(\tau_{kl} \left| \tau_{(k-1)l}\right.\right) p\left(\phi_{kl}\right) \quad (19)$$

It is very important to mention that the equations above are only valid if the time and angle distributions are independent.

Fig. 17 presents the arrival angles of clusters and rays in function of their corresponding arrival times. In Fig. 17(a) we can observe that the arrival time and angle of the clusters are not correlated. A higher time of arrival does not imply higher or lower angles of arrival.

The decorrelation between the two variables can also be noticed from the fact that a low inter-correlation is obtained between the times and angles of arrival of the clusters. If we analyze the rays, the same comments can be made (Fig. 17(b)), the times and angles of arrival rays are uncorrelated. As it is also stated in [36], since there is no significant correlation between time and angle, the density functions can be approximately separable.

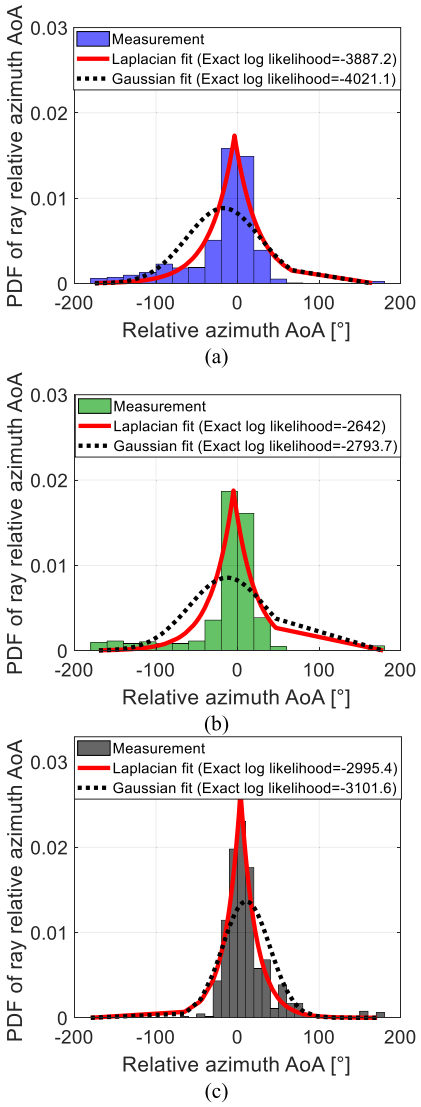

FIGURE 15. Relative arrival angle of the rays for: (a) *Indoor 1*, (b) *Indoor 2* and (c) *Indoor 3* scenarios.

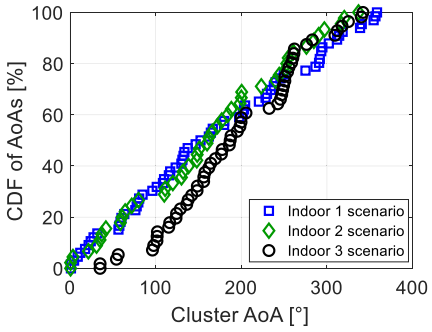

FIGURE 16. Clusters' AoA distribution.

As a conclusion, since we have a decorrelation between times and angles of arrival for both the clusters and rays, for simplifying the model implementation we can adopt (18)-(19).

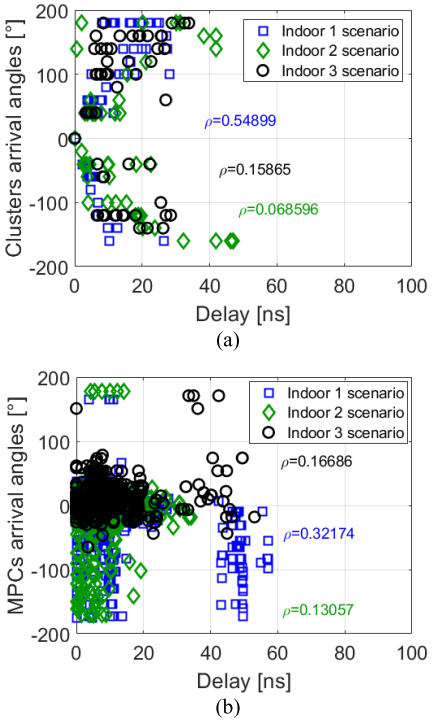

FIGURE 17. Representation of: (a) arrival times versus arrival angles of clusters and (b) arrival times versus arrival angles of rays for all indoor scenarios.

B. NLOS SCENARIOS

1) BLOCKING BY HUMAN BODY IN INDOOR 1 SCENARIO

Fig. 18 presents the MPCs extracted from the LOS and NLOS scenarios at 3.4m distance in between the antennas. Only the azimuthal angles of arrival have been considered because all measurements have been performed in the azimuth plane. As seen, when the phantom was placed in between the transmitter and receiver, the LOS component at 0° was obstructed (Fig. 18(b)).

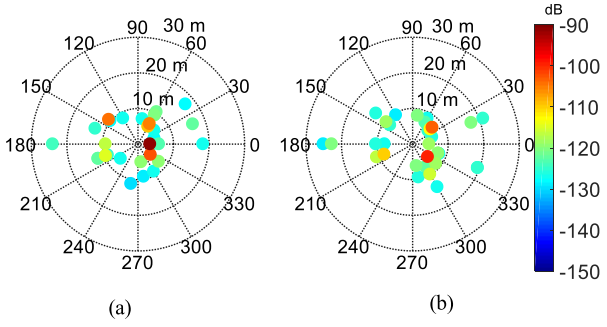

FIGURE 18. MPCs vs AoAs: (a) without and (b) with phantom in the *Indoor 1* laboratory environment.

Fig. 19 compares the omnidirectional power delay profile (PDP) along with the detected multipath measured in the LOS and NLOS scenarios for the *Indoor 1* scenario. The dotted line represents the threshold for the MPCs detection and it was chosen 20 dB above the noise floor level of

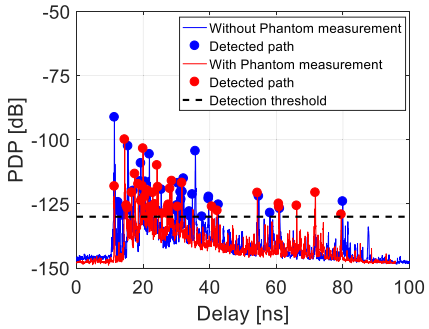

FIGURE 19. Example of PDP for the LOS/NLOS *Indoor 1* scenario.

the VNA. We can see that the main NLOS path is attenuated by 27 dB in comparison with the LOS path and that certain secondary paths are conserved for the NLOS scenario.

As the distance between the antenna increases, the obstruction and diffraction around the body changes, leading to a different effect on the main direct path. Still, secondary MPCs exist in both the LOS and NLOS cases. The secondary paths can yield an important energy contribution so when we integrate it with all MPCs we obtain a small increase in the path loss.

By comparison, between the NLOS and LOS scenarios, we obtained an increase of 6.2 dB for the path loss (Fig. 20(a)). The delay spread is also slightly augmented of about 1.7 ns as observed in Fig. 20(b) and the angular spread increased by about 20°(Fig. 20(c)).

2) BLOCKING BY WALL/DOOR IN INDOOR 3 SCENARIO

Similarly, in this section, we analyze the results obtained in the NLOS scenarios considering the obstruction from a wall/door in an office environment (*Indoor 3* scenario). The results are also compared with the LOS case. For the NLOS wall scenario, the shortest separation in between the receiver and transmitter was 1 m and for the NLOS door scenario, it was 1.3 m.

Based on the measurement results, the path loss and delay spread models were determined in a different manner, using an intercept point model with a breaking point as described below:

$$\begin{cases} PL1\,(d)\,[dB] = PL_{01} + 10 \cdot n_1 \cdot \log_{10}\left(\dfrac{d}{d_0}\right) \\ \qquad\qquad + X_{\sigma 1}, \quad d \le d1 \\ PL2\,(d)\,[dB] = PL_{02} + 10 \cdot n_2 \cdot \log_{10}\left(\dfrac{d}{d_1}\right) \\ \qquad\qquad + X_{\sigma 2}, \quad d > d1 \end{cases} \tag{20}$$

$$\begin{cases} \tau_{rms1}[ns] = a1 \cdot \left(\dfrac{d}{d_0}\right) + b1, \quad d \le d1 \\ \tau_{rms2}\,[ns] = a2 \cdot \left(\dfrac{d}{d_1}\right) + b2, \quad d > d1 \end{cases} \tag{21}$$

where PL_0 represents the intercept point at $d_0 = 1$ m, n is the path loss exponent, d is the exact measurement distance in between the transmitter and the receiver, d1 represents the starting measurement distance in between Tx and Rx (here 1 m for the wall scenario and 1.3 m for the door scenario), X_σ represents the path loss standard deviation, a is the delay spread exponent and b represents the standard deviation.

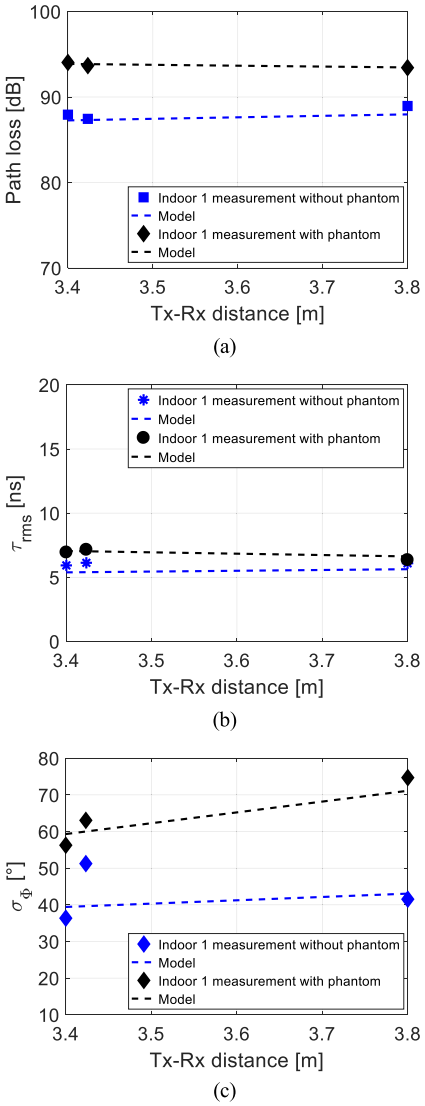

FIGURE 20. NLOS for *Indoor 1* scenario without/with phantom: (a) path loss, (b) delay spread and (c) angular spread.

Fig. 21(a) presents the path loss model measured in NLOS conditions. An increase around 27.3 dB in path loss is observed for the blockage by door in comparison with the blockage by wall. This is explained by the fact that a thin metallic sheet, which has higher attenuation than plasterboard, composes the door also. The delay spread, represented in Fig. 21(b), shows an increase of about 12 ns for the door scenario in comparison with the wall scenario. Note that the delay spread is quite constant along distance and that the slight decrease is due to the fitting effect that can be neglected. The slight increase in path loss and delay spread is due to the door composition. The wall plasterboard composition allows

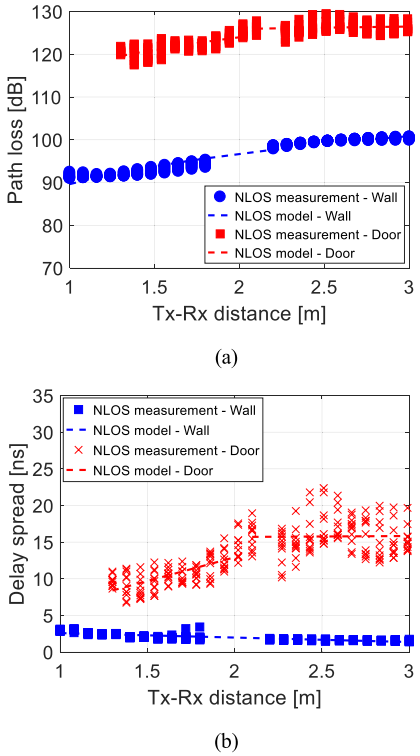

FIGURE 21. NLOS for *Indoor 3* scenario: (a) path loss and (b) delay spread.

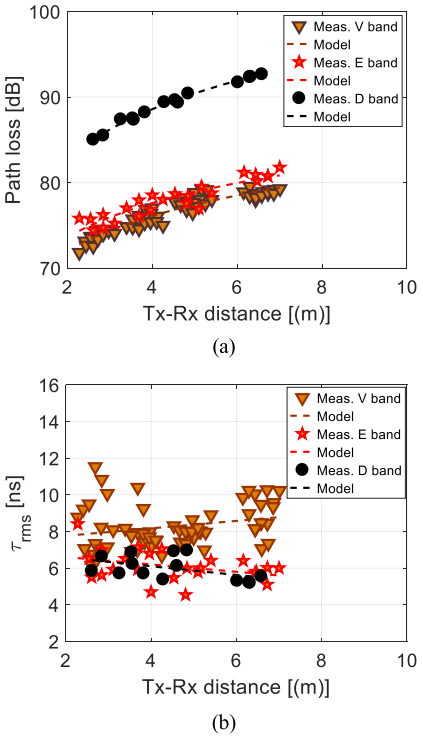

FIGURE 22. Representation of: (a) path loss and (b) delay spread for different frequency bands in *Indoor 3* scenario.

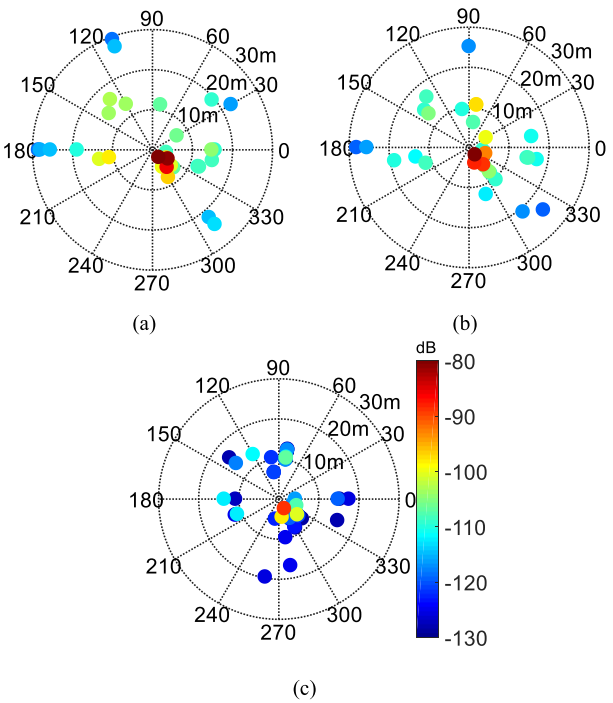

FIGURE 23. Representation of identified paths at: (a) 59-65 GHz, (b) 80.5-86.5 GHz, and (c) 126-156 GHz.

the main path to be less attenuated in comparison to the NLOS door case, which results in a small variation of the delay spread.

IV. COMPARISON WITH OTHER MM-WAVE CHANNELS

In this section, we compare the results obtained in D-band with those previously obtained in the V (59 - 65 GHz) and E (80.5 - 86.5 GHz) bands considering the *Indoor 3* scenario [18].

By comparing, the results obtained in the sub-THz channel with those obtained at mm-Wave frequencies in Fig. 22, one can notice that the path loss is 10 dB higher for the sub-THz model and that the delay spread is comparable with the E band measurement.

In Fig. 23 we present the different detected paths with their specific characteristics for *Indoor 3* scenario in different frequency bands and at the same position of the receiver and transmitter. We can notice that some common paths are detected even if the measurements were carried out at two different moments in time. The LOS components and some closer paths are identified but some secondary MPCs have a smaller energy contribution for the D band measurement. In V band, some paths between 20 and 30 m can be detected but at higher frequencies the same paths cannot be seen anymore. The amplitude of the secondary MPCs also decreased, lower than 20 dB for the sub-THz LOS case.

The results highlighted that the LOS path brings an important energy contribution in comparison with channels below 100 GHz. If we compare the model presented by us with IEEE 802.15.3c [1] at 60 GHz, we can remark some differences. The IEEE 802.15.3c channel model presented a path loss exponent between 1.16 and 1.53 while here, a higher path loss exponent (in between 1.45 and 1.93) was obtained.

The standard deviation for the 60 GHz channel in IEEE 802.15.3c was of 1.5 dB and 8.6 dB in the residential and office environments while here is lower (about maximum 0.6 dB).

Moreover, our measured exponential decay of clusters is lower (below 10 ns) than that of the IEEE 802.15.3c that varied between 4.46 ns and 41.9 ns in the residential environment and from 19.44 ns to 109.2 ns in the office scenario.

V. CONCLUSION

In this paper we proposed a channel characterization in D-band, for different indoor scenarios.

With respect to literature, this work addresses larger distances up to 10.6 meters. It also provides insights on large-scale parameters as well as on inter- and intra- cluster characteristics, which are not reported in literature.

As expected the Line of Sight component yields an important energy contribution. However secondary multipath components are still present, resulting in a delay spread up to 15 ns and angular spread in the order of 30° and 50°. Up to 5 time-overlapping clusters can be detected. These clusters are generally uniformly distributed in angular domain, while the inter-cluster rays have a Laplacian distribution.

Different obstructing conditions were also considered. While obstruction by door and wall strongly depends on the material characteristics, the human body obstruction presents attenuation that is very close to that already witnessed below 100 GHz. Therefore, knife-edge diffraction model, that is usually considered for NLOS scenarios, could be successfully exploited also in the sub-THz band [37].

In these scenarios beamforming approaches [38], [39] should be able to exploit secondary MPCs which are not obstructed. Thus, given the high losses and potential obstructions in this band, high gain beamforming antennas would be required.

REFERENCES

[1] *IEEE Standard for Information technology– Local and metropolitan area networks– Specific requirements– Part 15.3: Amendment 2: Millimeter-wave-based Alternative Physical Layer Extension*, Standards 802.15.3c-2009 IEEE Computer Society, Oct. 2009.

[2] A. A. M. Saleh and R. Valenzulea, "A statistical model for indoor multipath propagation," *IEEE J. Sel. Areas Commun.*, vol. SAC-5, no. 2, pp. 128–137, Feb. 1987.

[3] A. Maltsev, R. Maslennikov, A. Sevastyanov, A. Lomayev, and A. Khoryaev, "Statistical channel model for 60 GHz WLAN systems in conference room environment," in *Proc. 4th Eur. Conf. Antennas Propag.*, Apr. 2010, pp. 12–16.

[4] L. Raschkowski, P. Kyösti, K. Kusume, T. Jämsä, V. Nurmela, A. Karttunen, A. Roivainen, T. Imai, J. Järveläinen, J. Medbo, J. Vihriälä, J. Meinilä, K. Haneda, V. Hovinen, J. Ylitalo, N. Omaki, A. Hekkala, R. Weiler, and M. Peter, "METIS channel models," METIS Project, Deliverable D1.4, Jul. 2015.

[5] A. Maltsev, A. Pudeyev, I. Bolotin, G. Morozov, I. Karls, M. Faerber, I. Siaud, A.-M. Ulmer-Moll, J.-M. Conrat, R. J. Weiler, M. Peter, and W. Keusgen, "D5.1 channel modeling and characterization," MiWeBA Project, Deliverable D5.1, Jun. 2014.

[6] M. Peter, K. Haneda, S. L. H. Nguyen, A. Karttunen, J. Järveläinen, A. Bamba, R. D'Errico, J. Medbo, F. Undi, S. Jaeckel, N. Iqbal, J. Luo, M. Rybakowski, C. Diakhate, J.-M. Conrat, A. Naehring, S. Wu, A. Goulianos, and E. Mellios, "Measurement results and final mmMAGIC channel models," mmMAGIC Project, Deliverable D2.2, May 2017.

[7] T. S. Rappaport, G. R. Maccartney, M. K. Samimi, and S. Sun, "Wideband millimeter-wave propagation measurements and channel models for future wireless communication system design," *IEEE Trans. Commun.*, vol. 63, no. 9, pp. 3029–3056, Sep. 2015.

[8] *Study on Channel Model For Frequencies From 0.5 to 100 GHz*, document 3GPP TR 38.901 V15.0.0 (2018-06), 3rd Generation Partnership Project (3GPP), 2018.

[9] F. Sheikh, N. Zarifeh, and T. Kaiser, "Terahertz band: Channel modelling for short-range wireless communications in the spectral windows," *IET Microw., Antennas Propag.*, vol. 10, no. 13, pp. 1435–1444, Oct. 2016.

[10] N. Khalid and O. B. Akan, "Wideband THz communication channel measurements for 5G indoor wireless networks," in *Proc. IEEE Int. Conf. Commun. (ICC)*, Kuala Lumpur, May 2016, pp. 1–6.

[11] S. Kim and A. G. Zajić, "Statistical characterization of 300-GHz propagation on a desktop," *IEEE Trans. Veh. Technol.*, vol. 64, no. 8, pp. 3330–3338, Aug. 2015.

[12] S. Kim and A. Zajić, "Statistical modeling and simulation of short-range device-to-device communication channels at sub-THz frequencies," *IEEE Trans. Wireless Commun.*, vol. 15, no. 9, pp. 6423–6433, Sep. 2016.

[13] S. Priebe, C. Jastrow, M. Jacob, T. Kleine-Ostmann, T. Schrader, and T. Kurner, "Channel and propagation measurements at 300 GHz," *IEEE Trans. Antennas Propag.*, vol. 59, no. 5, pp. 1688–1698, May 2011.

[14] S. Priebe, M. Jacob, and T. Kuerner, "AoA, AoD and ToA characteristics of scattered multipath clusters for THz indoor channel modeling," in *Proc. 17th Eur. Wireless 2011—Sustain. Wireless Technol.*, Vienna, Austria, Apr. 2011, pp. 1–9.

[15] S. Priebe, M. Jacob, and T. Kürner, "Affection of THz indoor communication links by antenna misalignment," in *Proc. 6th Eur. Conf. Antennas Propag. (EUCAP)*, Prague, Mar. 2012, pp. 483–487.

[16] S. Kim, W. T. Khan, A. Zajić, and J. Papapolymerou, "D-band channel measurements and characterization for indoor applications," *IEEE Trans. Antennas Propag.*, vol. 63, no. 7, pp. 3198–3207, Jul. 2015.

[17] K. Haneda, J. Järveläinen, A. Karttunen, M. Kyrö, and J. Putkonen, "A statistical spatio-temporal radio channel model for large indoor environments at 60 and 70 GHz," *IEEE Trans. Antennas Propag.*, vol. 63, no. 6, pp. 2694–2704, Jun. 2015.

[18] A. Bamba, F. Mani, and R. D.'Errico, "Millimeter-wave indoor channel characteristics in V and E bands," *IEEE Trans. Antennas Propag.*, vol. 66, no. 10, pp. 5409–5424, Oct. 2018.

[19] *Standard Gain Horn, Model 29240-20*, Flann Microw.

[20] *EM—PHANTOM, TORSO-OTA-EV5.1 and TORSO-OTA-3TO6EV5.1*, Schmid Partner Eng., Torrance, CA, USA.

[21] M. Peter, M. Wisotzki, M. Raceala-Motoc, W. Keusgen, R. Felbecker, M. Jacob, S. Priebe, and T. Kürner, "Analyzing human body shadowing at 60 GHz: Systematic wideband MIMO measurements and modeling approaches," in *Proc. 6th Eur. Conf. Antennas Propag.*, Prague, Czech Republic, Mar. 2012, pp. 468–472.

[22] M. Jacob, S. Priebe, R. Dickhoff, T. Kleine-Ostmann, T. Schrader, and T. Kurner, "Diffraction in mm and sub-mm wave indoor propagation channels," *IEEE Trans. Microw. Theory Techn.*, vol. 60, no. 3, pp. 833–844, Mar. 2012.

[23] C. Gustafson and F. Tufvesson, "Characterization of 60 GHz shadowing by human bodies and simple phantoms," in *Proc. 6th Eur. Conf. Antennas Propag. (EUCAP)*, Mar. 2012, pp. 473–477.

[24] M. Jacob, S. Priebe, A. Maltsev, A. Lomayev, V. Erceg, and T. Kürner, "A ray tracing based stochastic human blockage model for the IEEE 802.11ad 60 GHz channel model," in *Proc. 5th IEEE Eur. Conf. Antennas Propag. (EUCAP)*, Rome, Italy, Apr. 2011, pp. 3084–3088.

[25] M. Cheffena, "Physical-statistical channel model for signal effect by moving human bodies," *EURASIP J. Wireless Commun. Netw.*, vol. 2012, p. 77, Mar. 2012.

[26] M. Jacob, C. Mbianke, and T. Kurner, "A dynamic 60 GHz Radio Channel Model for system Level Simulations with MAC protocols for IEEE 802.11ad," in *Proc. IEEE Int. Symp. Consum. Electron. (ISCE)*, Braunschweig, Germany, Jun. 2010, pp. 1–5.

[27] S. M. Yano, "Investigating the ultra-wideband indoor wireless channel," in *Proc. IEEE 55th Veh. Technol. Conf.*, Birmingham, AL, USA, vol. 3, May 2002, pp. 1200–1204.

[28] L. Rubio, J. Reig, H. Fernández, and V. M. Rodrigo-Peñarrocha, "Experimental UWB propagation channel path loss and time-dispersion characterization in a laboratory environment," *Int. J. Antennas Propag.*, vol. 2013, Mar. 2013, Art. no. 350167.

[29] J. Ahmadi-Shokouh and R. C. Qiu, "Ultra-wideband (UWB) communications channel measurements-a tutorial review," *Int. J. Ultra Wideband Commun. Syst.*, vol. 1, no. 1, pp. 11–31, 2009.

[30] N. Czink, "The random cluster model—A stochastic MIMO channel model for broadband wireless communication systems of the 3rd generation and beyond," Ph.D. dissertation, Technische Universität Wien, Vienna, Austria, 2007.

[31] B. Neekzad, K. Sayrafian-Pour, and J. S. Baras, "Clustering characteristics of millimeter wave indoor channels," in *Proc. IEEE Wireless Commun. Netw. Conf.*, Mar./Apr. 2008, pp. 1217–1222.

[32] M. R. Akdeniz, Y. Liu, M. K. Samimi, S. Sun, S. Rangan, and E. Erkip, "Millimeter wave channel modeling and cellular capacity evaluation," *IEEE J. Sel. Areas Commun.*, vol. 32, no. 6, pp. 1164–1179, Jun. 2014.

[33] S. Hur, Y.-J. Cho, J. Lee, N.-G. Kang, J. Park, and H. Benn, "Synchronous channel sounder using horn antenna and indoor measurements on 28 GHz," in *Proc. IEEE Int. Black Sea Conf. Commun. Netw. (BlackSeaCom)*, May 2014, pp. 83–87.

[34] A. Davydov, A. Maltsev, and A. Sadri, "Saleh-Valenzuela Channel Model Parameters for Library Environment," in *Proc. IEEE Work. Group Wireless Pers. Area Netw. (WPANs)*, Jul. 2006, p. 802.15-06.

[35] A. F. Molisch, "Ultrawideband propagation channels-theory, measurement, and modeling," *IEEE Trans. Veh. Technol.*, vol. 54, no. 5, pp. 1528–1545, Sep. 2005.

[36] Q. H. Spencer, B. D. Jeffs, M. A. Jensen, and A. L. Swindlehurst, "Modeling the statistical time and angle of arrival characteristics of an indoor multipath channel," *IEEE J. Sel. Areas Commun.*, vol. 18, no. 3, pp. 347–360, Mar. 2000.

[37] T. S. Rappaport, G. R. MacCartney, Jr., S. Sun, H. Yan, and S. Deng, "Small-scale, local area, and transitional millimeter wave propagation for 5G communications," *IEEE Trans. Antennas Propag.*, vol. 65, no. 12, pp. 6474–6490, Nov. 2017.

[38] M. Mantash and T. A. Denidni, "CP antenna array with switching-beam capability using electromagnetic periodic structures for 5G applications," *IEEE Access*, vol. 7, pp. 26192–26199, 2019.

[39] M. Mantash, A. Kesavan, and T. A. Denidni, "Beam-tilting endfire antenna using a single-layer FSS for 5G communication networks," *IEEE Antennas Wireless Propag. Lett.*, vol. 17, pp. 29–33, 2018.

L. POMETCU received the B.E. degree in electronics, telecommunications, and information technology and the master's degree in mobile communications from the Politehnica University of Bucharest, Romania, in 2011 and 2013, respectively, and the Ph.D. degree in signal processing and telecommunications from the Institute of Electronics and Telecommunications of Rennes (IETR), University of Rennes 1, Rennes, France, in 2016.

Since 2016, she has been a Research Engineer with the CEA-LETI, Grenoble, France. Her current research interests include radio channel modeling for outdoor and indoor scenarios, radio channel measurements, over-the-air techniques, material characterization, antenna design, metamaterials and frequency selective surface (FSS) designs, radar cross section, and signal treatment.

Dr. Pometcu was a recipient of the Best Poster Award from the Conference on Microwave Materials and Their Applications (MMA), in 2016.

R. D'ERRICO (SM'19) received the Laurea degree in telecommunications engineering from the University of Bologna, Italy, in 2005, and the Ph.D. degree in physics from the University of Orsay, Paris, France, and in electronics, information, and telecommunication engineering from the University of Bologna.

Since 2008, he has been a Senior Scientist and Project Manager at the CEA-LETI Grenoble, France. His research interests include radio channel sounding and modeling, antenna design and characterization, mm-wave technologies, body area networks (BANs), UWB and UHF RFID, localization, cooperative communication protocols, OTA tests, and radar.

Dr. D'Errico was a French Delegate Member of the IRACON action on 5G and beyond communications. He received three Best Paper Awards, including the IEEE PIMRC 2009, IFIP NTMS 2011, and LAPC 2012 Best Student Paper. He participated to COST actions 2100 and IC1004, where he served as the Chair of the Working Group on "Body Environment."